Applied Catalysis B: Environmental 240 (2019) 112–121

Contents lists available at ScienceDirect

Applied Catalysis B: Environmental

journal homepage: www.elsevier.com/locate/apcatb

Atomic Co/Ni dual sites and Co/Ni alloy nanoparticles in N-doped porous Janus-like carbon frameworks for bifunctional oxygen electrocatalysis

Zehui Li[a,b,1], Hongyan He[b,1], Hongbin Cao[b], Shaoming Sun[c], Wenlin Diao[c], Denglei Gao[b], Peilong Lu[b], Shuangshuang Zhang[d], Zhuang Guo[b,c], Mingjie Li[e], Rongji Liu[b,f], Dunhao Ren[b], Chenming Liu[b], Yi Zhang[b], Zheng Yang[g], Jingkun Jiang[a], Guangjin Zhang[b,*]

[a] State Key Joint Laboratory of Environment Simulation and Pollution Control, School of Environment, Tsinghua University, Beijing, 100084, PR China
[b] CAS Key Laboratory of Green Process and Engineering, Beijing Engineering Research Center of Process Pollution Control, Institute of Process Engineering, Chinese Academy of Sciences, Beijing, 100190, PR China
[c] University of Chinese Academy of Sciences, Beijing, 100049, PR China
[d] College of Chemistry, Chemical Engineering and Materials Science, Collaborative Innovation Center of Functionalized Probes for Chemical Imagining Universities of Shandong, Key Laboratory of Molecular and Nano Probes, Ministry of Education, Institute of Molecular and Nano Science, Shandong Normal University, Jinan, 250014, PR China
[e] CAS Key Laboratory of Bio-based Materials, Qingdao Institute of Biomass Energy and Bioprocess Technology, Chinese Academy of Sciences, Qingdao, 266101, PR China
[f] Institute of Inorganic Chemistry I, Ulm University, Ulm, 89081, Germany
[g] School of Printing & Packaging, Beijing Institute of Graphic Communication, Beijing, 102600, PR China

ARTICLE INFO

Keywords:
Atomic
Dual sites
Electrocatalysts
Oxygen reduction reaction
Oxygen evolution reaction

ABSTRACT

Single-atom electrocatalysts have attracted board interest in the recent years as they combine the advantages of heterogeneous and homogeneous electrocatalysts. Nevertheless, single-atom electrocatalysts with single metal component cannot further satisfy the demand of catalytic properties. This work developed atomic Co/Ni dual sites in N-doped porous carbon Janus-like frameworks through epitaxial growth of cobalt based MOFs on nickel complexes. Structural characterization and atomic-scale transmission electron microscopy revealed the homogeneously dispersed active sites of Co-Ni alloy and single Co/Ni atoms. Electrochemical data strongly demonstrated the advantages of integrating Co-MOF and Ni complex with different topological structures to form a Janus-like structure. The resultant catalysts afforded onset potential of 0.93 V and half-wave potential of 0.84 V for oxygen reduction reaction in alkaline media, and 0.86 V and 0.73 V in acid media, which is better than single noble-metal-free catalysts, even close to commercial Pt/C. Besides, the catalysts also exhibited good oxygen evolution reaction performance (a current density of 10 mA cm^{-2} at a potential of 1.59 V) and overvoltage between ORR and OER is 0.78 V. Density functional theory calculations indicated the high electrocatalytic activities are originated from the synergetic effect of atomic Co/Ni-*N*-C bonds and microstructure of the prepared materials. This work paves a new avenue for the development of multiatomic electrocatalysts for energy conversion.

1. Introduction

Oxygen reduction reaction (ORR) and oxygenevolution reaction (OER) are two important half reactions in renewable-energy technologies such as fuel cells and metal-air batteries [1–3]. The catalysts for oxygen reactions play key roles and are major obstacles limiting the practical application of these technologies. Traditionally, noble metals such as Pt were the commercial catalyst for its high catalytic activity in ORR and OER [4–6]. However, their scarcity status and poor stability limited large scale applications of the technologies [7,8]. Therefore, to develop noble-metal free ORR and OER electrocatalysts with good stability and catalytic performance remains urgent and challenging [9,10].

To date, various non-precious metals such as cobalt, iron, nickel, copper and manganese have been developed to be oxygen electrocatalysts [11–13]. However, high surface energies of these non-precious metals will form nanoparticles to limit their catalytic activities [14–16]. Homogeneously dispersed single atomic (SA) catalyst is an efficiently

* Corresponding author.
E-mail address: zhanggj@ipe.ac.cn (G. Zhang).
[1] These authors contributed equally.

https://doi.org/10.1016/j.apcatb.2018.08.074
Received 5 June 2018; Received in revised form 23 August 2018; Accepted 28 August 2018
Available online 31 August 2018
0926-3373/

avenue to avoid aggregation of metals [17,18], SA catalysts can surpass the traditional nanoparticles in performance owing to their atomic level configurations, and the dispersed SAs will increase the number of active sites and surface area significantly [19,20]. Metal-organic-frameworks (MOFs) have emerged as precursors for synthesis of SA catalysts with good ORR and OER performance [21–23]. As a result of the specific organic and inorganic structure of MOFs, which can anchor and disperse metals in the carbon frameworks to form atomically dispersed metal sites [24–26]. In all MOFs, N-riched zeolitic imidazolate frameworks (ZIFs) is a typical sacrificial templates in preparing single metal atoms and N-doped carbon materials through pyrolysis [26,27]. The transition metals (mostly Zn and Co) in the frameworks can interact with N and C atoms and form the homogeneous phase of transition metal-nitrogen-carbon (M-N-C, where M usually means Zn or Co) as active sites [28–30]. However, electrocatalytic activities of these single ZIF-derived carbon materials toward ORR and OER are not satisfied and need to be improved [31]. To overcome this limit, various strategies have been developed to finely adjust the composition and structure hierarchy, aiming to optimize the electrocatalysis properties [32,33]. For instance, multi-metallic M-N-C (e.g. M is Fe, Ni or Co) catalysts were synthesized from core-shell structured ZIFs composites through epitaxial growth methods, which can efficiently enhance the synergistic effect between metal-metal and metal-N species in carbon frameworks [34–36]. Therefore, delicate design and synthesis of ZIFs possess multimetallic active sites and extraordinary structures can achieve different physical and chemical properties [37–40]. Recent reports suggested that ORR activity of transition metals follows the order of Fe > Co > Cu > Mn > Ni, and OER activity follows the order of Cu, Mo, Mn, Fe > Ni > W > Zn > Cr > Co [41,42]. Moreover, the synergistic effect between different phases of metals can efficiently improve the ORR and OER activities [43]. Thus, the selection of metals for ORR/OER bifunctional catalysts is significant. Despite Fe may have better ORR/OER activity than Ni and Co, Fe has lower conductivity and stability than Co/Ni and is probably solved in the solution during the reaction [44,45]. In addition, recent reports suggested that Co and Ni are transition metals with strong capability to develop bimetallic alloy systems for diverse catalytic applications, especially in ORR and OER [46,47].

Keeping in view the challenges of achieving highly concentrated and uniformly dispersed atomic metal sites, we developed universal and effective strategy for designing multiatomic Janus-like electrocatalysts. In this contribution, atomic Co/Ni dual sites dispersed N-doped porous carbon Janus-like frameworks as efficient electrocatalyst for oxygen reactions were synthesized. The synthesized catalysts possess two different topologies and form large quantity of homogeneous Co/Ni atomistic sites, which are beneficial to the electrocatalytic performance. As expected, the prepared electrocatalysts showed high electrocatalytic performance of ORR and OER, which were among the best in reported Pt-free catalysts.

2. Experimental sections

2.1. Materials

2.1.1. One step synthesis of tris-1,10-phenanthroline nickel(II) nitrate (PNi)

$Ni(NO_3)_2{\cdot}6H_2O$ (0.3 *g*) and 1,10-phenanthroline (0.54 *g*) were dissolved separately in 15 mL deionized water and stirred for 1 h under 70 °C. After that, the solution was centrifuged and washed with ice water. The obtained crystals were dried under room temperature.

2.1.2. ZIF-67 and Co-N/C

$Co(NO_3)_2{\cdot}6H_2O$ (0.4 *g*) and 2-methylimidazole (0.9 *g*) were dissolved in 30 mL methanol, respectively. Then they were mixed together and reaction for four hours. ZIF-67 powders could be collected after centrifugation and methanol washing. After that, coblat and nitrogen doped carbon (Co-N/C) was recieved by carbonizing ZIF-67 under the protection of nitrogen (750 °C for three hour) [26].

2.1.3. CoPNi-MOF and coblat, PNi and nitrogen tri-doped carbon (CoPNi-N/C)

$Co(NO_3)_2{\cdot}6H_2O$ (0.4 g) and PNi (0.06 g) were dissolved together in methanol (60 mL), then the solution is added into 30 mL 2-methylimidazole (0.9 g) methanol solution. After reaction for four hours, the CoPNi-MOF powders were recieved. Finally, CoPNi-N/C was recieved by carbonizing CoPNi-MOF under the protection of nitrogen (750 °C for three hour).

2.1.4. CoDNi-MOF and coblat, dimethylglyoxime nickel(II) (DNI) and nitrogen tri-doped carbon (CoDNi-N/C)

$Co(NO_3)_2{\cdot}6H_2O$ (0.4 g) and DNi (0.06 g) were dissolved together in methanol (60 mL), then the solution is added into 30 mL 2-methylimidazole (0.9 g) methanol solution. After reaction for four hours, the CoDNi-MOF powders were recieved. Finally, CoDNi-N/C was recieved by carbonizing CoDNi-MOF under the protection of nitrogen (750 °C for three hour).

2.2. Characterizations

The morphology of the samples were characterized by scanning electron microscopy (SEM, FEI Nova Nano- SEM 450, 5 kV), transmission electron microscopy (TEM, JEOL 2100 F, 100 kV) and high-angle annular dark-field scanning transmission electron microscope (HAADF-STEM, JEM-ARM200 F TEM/STEM, 200 kV). The structure of the samples were characterized by Raman spectroscopy (inVia-Reflex, 532 nm), nitrogen physical adsorption apparatus (Autosorb-IQ, Quantachrome, 77 K), X-ray diffraction (XRD, X' PERTPRO MPD) and X-ray photoelectron spectroscopy (XPS, ESCALab 250Xi).

2.3. Electrochemical measurements

Electrochemical workstation (CHI 760e, CH Instrument, Shanghai, China) and a three-electrode-system with work electrode (catalyst-modified glassy carbon electrode), reference electrode (Ag/AgCl) and counter electrode (platinum) are used to perform cyclic voltammetry (CV) and linear sweep voltammetry (LSV). In the loading procedure of electrocatalysts on rotating disk electrode (RDE)/ rotating ring-disk electrode (RRDE), RDE/RRDE were first polished to expose the fresh surface of glass carbon by Al_2O_3 powders (50 nm). Then 4.8 μL solution of electrocatalysts (4 mg catalysts dispersed in intermixture of 500 μL N,*N*-dimethylformamide, isothermal ultrasonic until achieve ink solution) were dropped onto GCE electrodes (loading amount is about 0.3 mg cm^{-2}). After that, 1 μL 0.5% Nafion alcohol solution were droped on the RDE/RRDE. Finally, the electrocatalysts modified RDE/RRDE were dried overnight. Rotating ring-disk electrode (RRDE) was performed to determine the number of electrons transferred (*n*) and H_2O_2 yield. During the test, the ring electrode was held at 1.2 V and 1.5 V vs. relative hydrogen electrode (RHE) in acid and basic condition, respectively. The *n* and H_2O_2 yield can be calculated by following equations.

$$n = \frac{4I_{disk}}{I_{ring}/N + I_{disk}}$$

$$H_2O_2\% = \frac{200I_{ring}/N}{I_{ring}/N + I_{disk}}$$

where N is the collection efficiency (40%), I_{disk} and I_{ring} are the voltammetric currents at the disk and ring electrodes, respectively.

RHE calibration of reference electrodes (saturated calomel electrode (SCE) and Ag/AgCl) were performed in acid (0.1 M $HClO_4$) and basic (0.1 M KOH) conditions, respectively. Pt wires were used as working electrode and counter electrode. The solution is fill with saturated

hydrogen. The CV scan rate was 1 mV s^{-1}. As shown in Fig. S1, the RHE could be calibrated by the average of the potentials of current crossed zero. So E (RHE) = E (SCE) + 0.312 V in 0.1 M $HClO_4$; E (RHE) = E (Ag/AgCl) + 0.949 V in 0.1 M NaOH.

All tests were performed current-resistance (*iR*) compensation for 85%.

2.4. Methodology and calculation model

To understand the nature of the high ORR reactivity of catalysts, Bader charge analysis (BCA) and charge density difference analysis (CDDA) [48] were performed by Vienna ab initio Simulation Package (VASP) [49]. The exchange-correlation functional of the Perdew – Burke – Ernzerhof (PBE) parameterization was calculated by the generalized gradient approximation [50,51]. The energy cutoff of plane-wave basis sets is 500 eV, and sampling k points of Brillouin zone integration used a 1 × 1 × 1 Monkhorst-Pack mesh grid. The convergence thresholds is 10^{-5} eV and energy and force is 0.01 eV/Å.

3. Results and discussion

3.1. The design of atomic Co/Ni dual sites in N-doped porous Janus-like carbon frameworks catalysts

ZIFs derived atomic Co/Ni dual sites immobilized N-doped porous carbon frameworks catalysts were fabricated as illustrated in Fig. 1A and B. Typically, ZIF-67 with dodecahedral framework was first synthesized by mixing Co(II) and 2-methylimidazole in methanol at room temperature. Then the Co-N/C was obtained by carbonizing ZIF-67 [52]. In order to prepare atomic Co/Ni dual sites catalyst, Ni precursors like 1,10-phenanthroline nickel(II) nitrate (PNi, Figs. S2, S3) or dimethylglyoxime nickel(II) (DNi) were introduced into the mixture of Co(II) and 2-methylimidazole during the reactions, and the composites were prepared through epitaxial growth. During this process, coordinated nickel ions in Ni complexes have competitive coordination effect with 2-methylimidazole. Thus nickel ions could gradually enter and be anchored into the framework by forming Ni—N—C bonds. The as-prepared Janus-like samples were named CoXNi-MOF and the corresponding carbonized materials are named CoXNi-N/C (XNi are PNi or DNi).

3.2. Characteristics and structure of atomic Co/Ni dual sites in N-doped porous Janus-like carbon frameworks catalysts

The SEM image of the carbonized ZIF-67 (Co-N/C) shows the typical dodecahedral shape with a size of 500 nm to 1 μm (Fig. 1C,D). After epitaxial growth of ZIF-67 on the surface of PNi, the SEM of corresponding CoPNi-N/C shows that dodecahedrons are closely packed together to form a kind of coralloid-like structure, and the size of individual dodecahedron remain invariability (Figs. 1E,F, S4A). In the case of CoDNi-N/C, however, those dodecahedrons are found to be buried in a kind of spongy-like structure (Figs. 1G,H, S4B), which is due to the porous structure of DNi. This indicates that the structure of Ni precursors and fabrication strategies play key roles in the determination

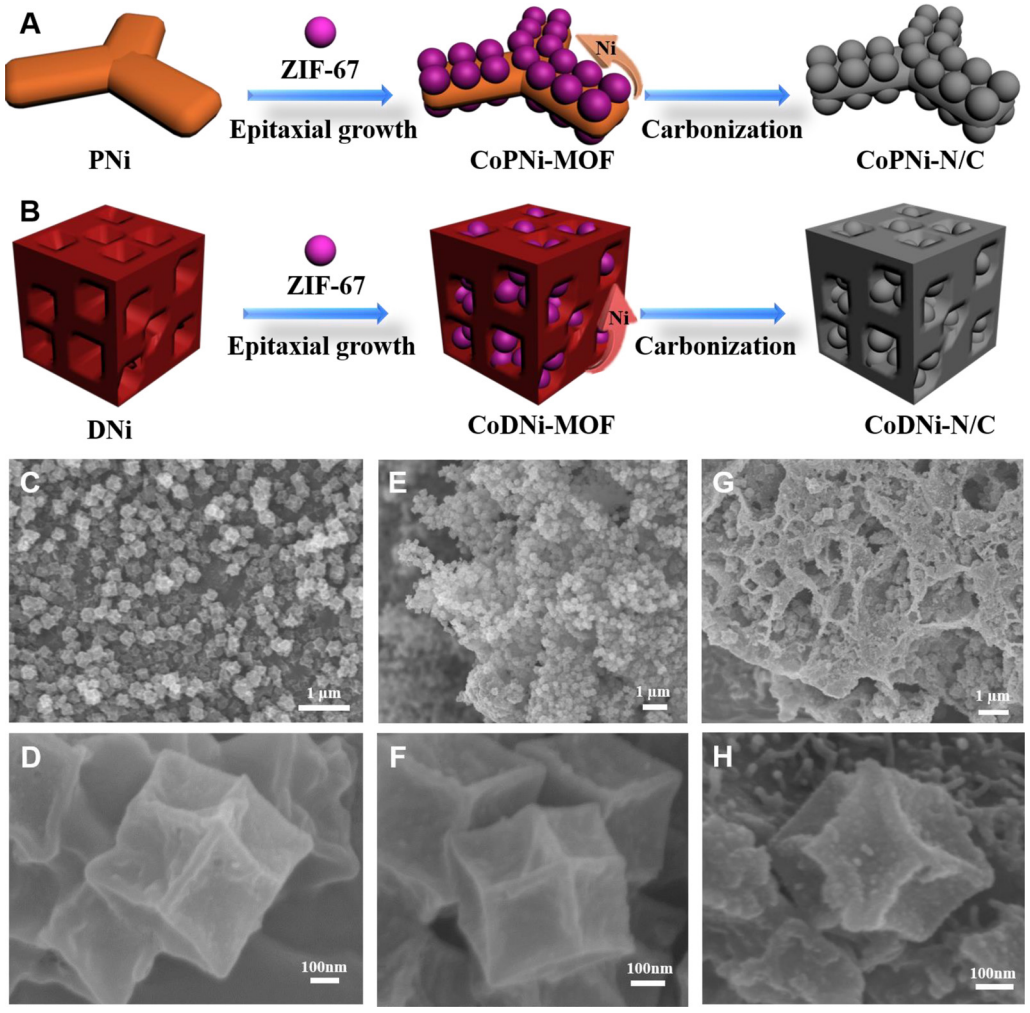

Fig. 1. Schematic illustration of the synthesis process for the (A) CoPNi-N/C and (B) CoDNi-N/C. SEM of (C,D) Co-N/C, (E,F) CoPNi-N/C and (G,H) CoDNi-N/C.

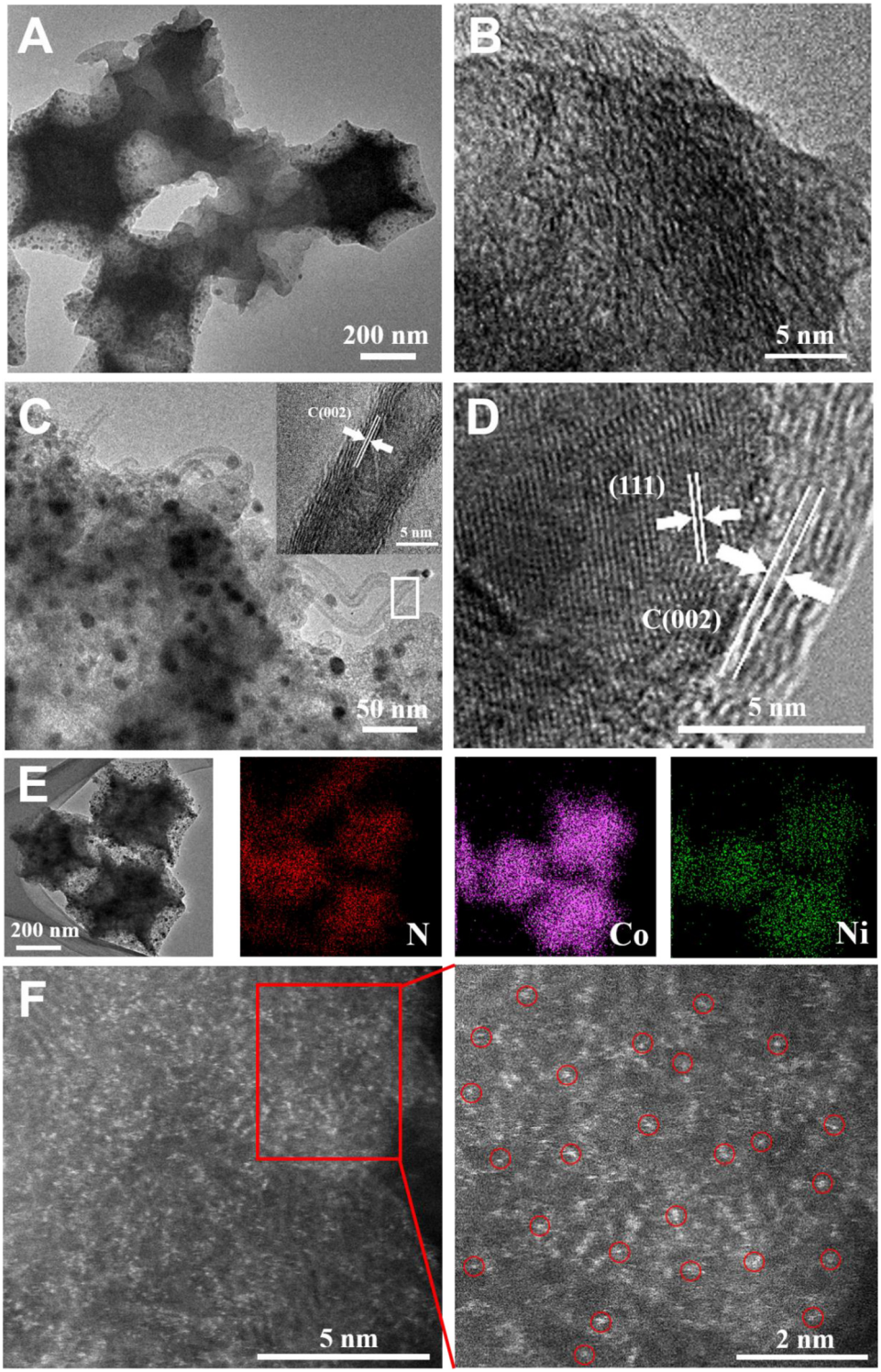

Fig. 2. TEM of (A,B,C,D) CoXNi-N/C (inset HRTEM corresponding to the area labeled I and II) and corresponding (E) elemental mappings of N, Co and Ni elements. (F) Magnified HAADF-STEM of CoXNi-N/C, showing atomic Co/Ni dual sites dominant in CoXNi-N/C.

of the final Janus-like structure with different topological structures, which are suggested to be influential on the interfacial interaction, electron transfer and catalytic performance.

The microstructures of the as-prepared catalysts were further investigated by TEM. For Co-N/C, typical dodecahedrons are observed with multiple Co nanoparticles of ~10 nm homogeneously embedded in the porous carbon framework. In addition, some broken holes can be seen clearly at the edge of the dodecahedrons due to escape of cobalt nanoparticles at high temperature (Fig. S5). After adding Ni complexes, the CoXNi-N/C shows morphology with dodecahedrons supported/connected by a kind of cloud-like carbons (Fig. 2A). With closer observation by TEM, micro-pores at edge of framework are found homogenously dispersed within the whole carbon matrix of CoXNi-N/C with distinct graphitic carbon domains and defect sites (Fig. 2B). Interestingly, a few carbon nanotubes (CNTs) with the lengths of several hundred nanometers and diameters of ~10 nm are wrapped around the

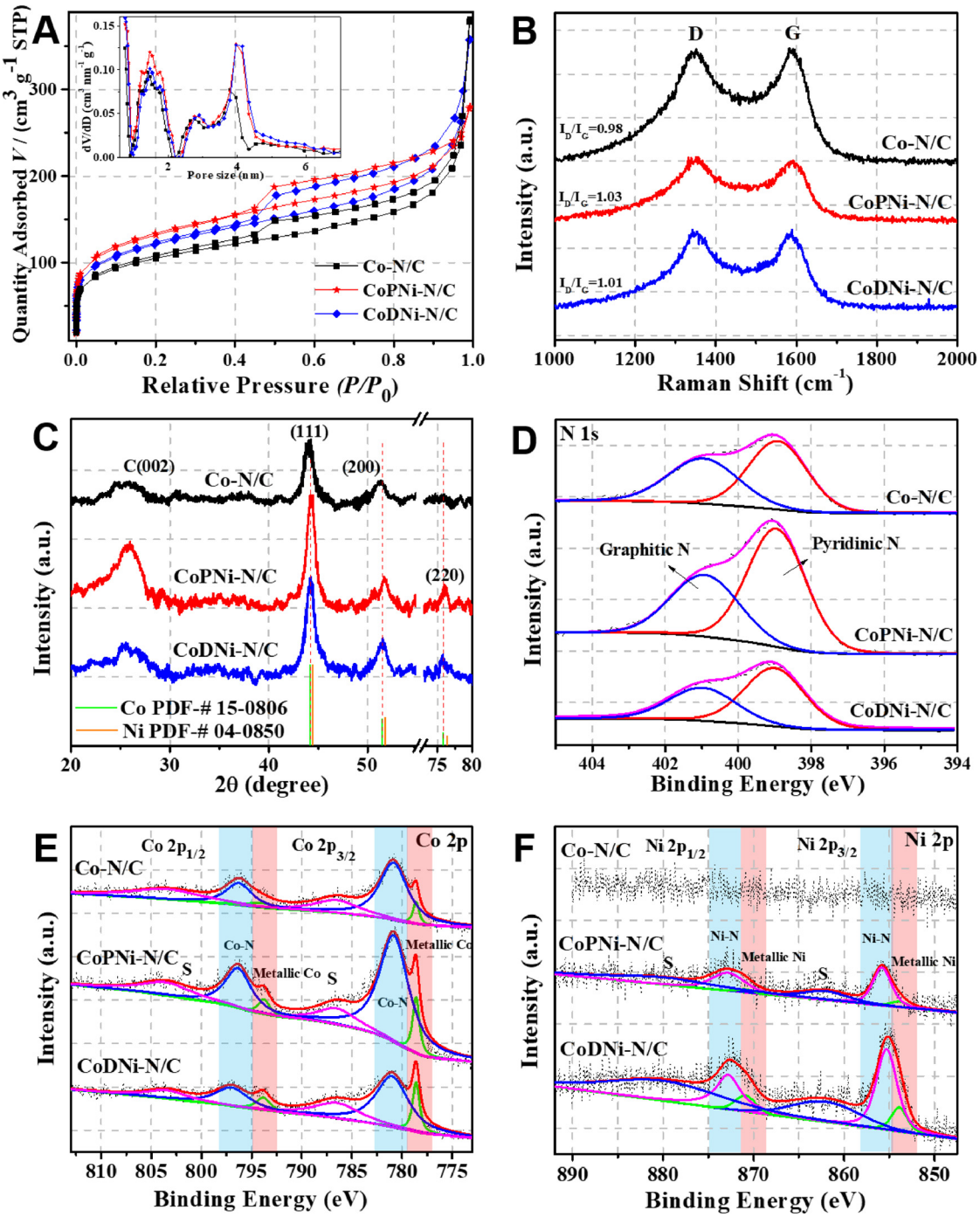

Fig. 3. (A) N_2 adsorption-desorption isotherms (inner is pore-size distributions), (B) Raman spectra, (C) wide-angle XRD patterns, high-resolution XPS spectra of (D) N 1 s, (E) Co 2p and (F) Ni 2p of Co-N/C, CoPNi-N/C and CoDNi-N/C.

polyhedral of CoXNi-N/C (Fig. 2C). These multi-wall CNTs are crystalline with an inter-planar distance of ~0.35 nm, corresponding to the C(002) plane. This could be further investigated by high resolution TEM (HRTEM) (Fig. 2D), the tip of the CNTs with an inter-planar distance of ~0.2 nm are seen on the surface of CoXNi-N/C, corresponding to the (111) plane of Co and Ni nanoparticles (the lattice spacing in the (111) plane of Co is 0.2047 nm and Ni is 0.2041 nm). The results suggests that Co-Ni alloy nanoparticles are capped at the tip of the CNTs that serves as the catalyst for growth of CNTs.

Co/Ni dual metallic Janus-like electrocatalyst (CoXNi-N/C) was further investigated by elemental mappings (Fig. 2E), which showed that all elements of N, Co and Ni are homogenously distributed in the framework. The results indicates that Ni ions are released into ZIF-67 steadily during its crystallization process, and thus form Co/Ni dual metallic Janus-like electrocatalyst. More importantly, the dark-field HAADF analysis showed that the aggregated and homogeneously distributed small bright dots, which are inferred to single atoms of Co/Ni throughout carbon frameworks (Fig. 2F).

The pore of the samples were exhibited by N_2 adsorption and desorption isotherms (Fig. 3A). The IV–type curves indicates that micropores and mesopores coexist in the materials. In the curves, the sharp uptakes at low relative pressure (< 0.05) indicated the presence of micro-pores. The hysteresis loops and gradual uptakes at a relative pressure range between 0.45 and 1 are caused by the capillary

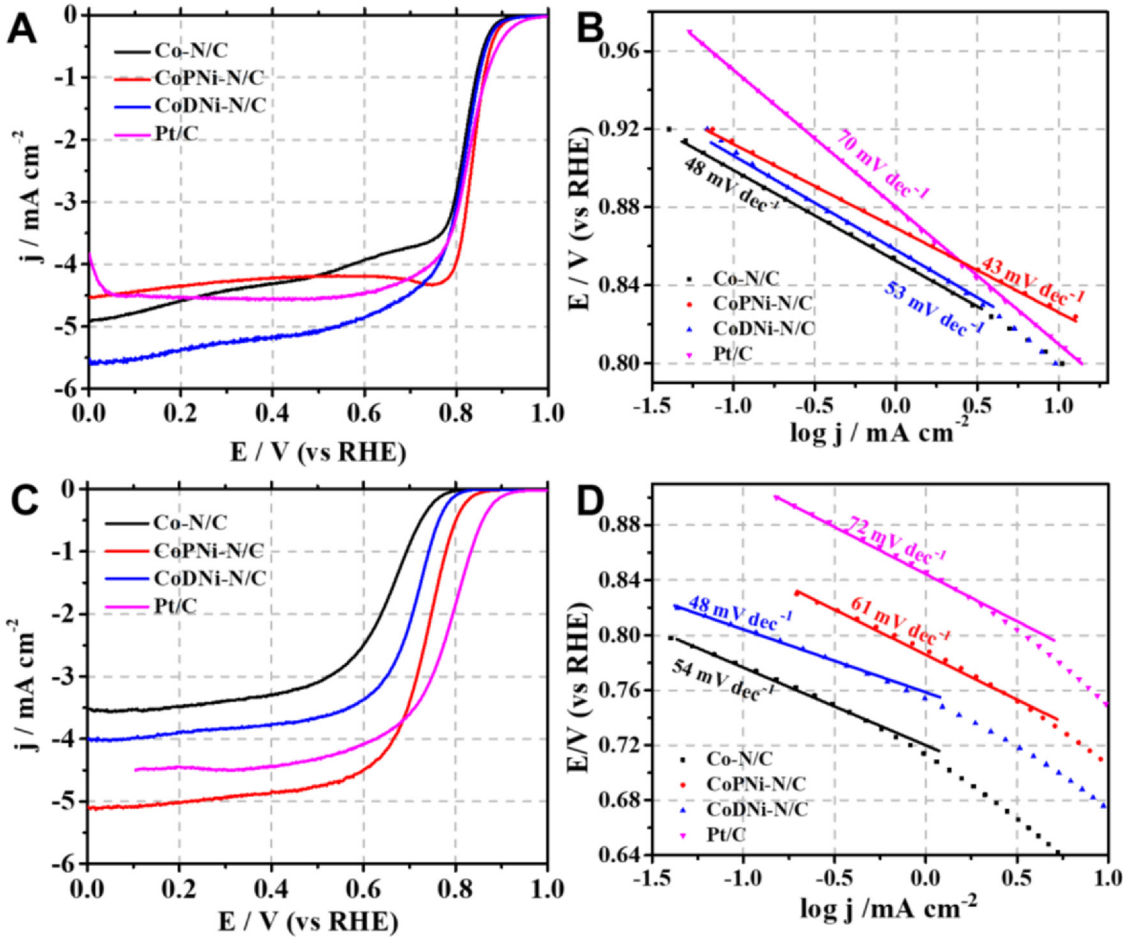

Fig. 4. LSV curves of Co-N/C, CoPNi-N/C, CoDNi-N/C and Pt/C in (A) O_2-saturated 0.1 M KOH solution and (C) 0.1 M $HClO_4$ solution at a rotation rate of 1600 rpm, and (B,D) corresponding Tafel plots.

condensation of N_2 in mesopores. Such hysteresis loops have often been observed in large mesoporous materials (e.g. carbonized ZIF-8@ZIF-67 [53]), and the loops are more distinct for the CoXNi-N/C. Base on Brunauer–Emmett–Teller (BET) analysis (Table S1), the calculated specific surface area (SSA) of Co-N/C (354.9 $m^2 g^{-1}$) is enlarged by combining PNi (446.8 $m^2 g^{-1}$ for CoPNi-N/C) and DNi (398.3 $m^2 g^{-1}$ for CoDNi-N/C). Density functional theory (DFT) calculation was further performed to determine pore size distribution of different catalysts. It can be seen that the resultant CoPNi-N/C and CoDNi-N/C show more micro-pores with the value of V_{mic}/V_t to be 41.72% and 27.06%, which are much larger than that of Co-N/C (22.40%). This result is in consistent with TEM observation which shows lots of micro-pores in CoXNi-N/C catalysts. The high content of micro-pores is beneficial to its absorption of oxygen and thus will be helpful for their electrocatalytic performance of ORR and OER.

Raman spectra (Fig. 3B) showed that the relative intensities of D and G bands (I_D/I_G) are increased from 0.98 (Co-N/C) to 1.03 (CoPNi-N/C) and 1.01 (CoDNi-N/C), indicating a lower degree of graphitization and higher content of defects in CoXNi-N/C. This can be ascribed to the higher micro-porosity as revealed by sorption isotherms, and also likely to be attributed to the etching effect of nickel during carbonization.

XRD is used to investigate the structure of catalysts. As shown in Fig. 3C, all samples exhibit similar XRD patterns with four identified peaks. These well-defined diffraction peaks at 25°, 44°, 51° and 75° are corresponding to (002) lattice plane of graphitic carbon, (111), (200) and (220) lattice planes of metallic Ni (JCPDS no. 04-0850) or Co (JCPDS no. 15-0806), respectively. In addition, it should be noted that the position of peaks corresponding to diffraction of Co or Ni in the synthesized materials are all moved to the middle of the standard position of metallic Co and Ni recorded in database, indicating Co-Ni alloys nanoparticles are formed [54].

XPS was used to investigate the chemical composition of the catalysts. The full XPS spectra reveals the presence and percentage of carbon, cobalt, nitrogen, oxygen and nickel species (Fig. S6), which are consistent with the XRD patterns. The N, Co content of CoXNi-N/C are higher than Co-N/C in varying degrees, and the O content of CoXNi-N/C is lower than Co-N/C. Specifically, the highest nitrogen content (10.29%) and lowest oxygen content (5.06%) are observed for CoPNi-N/C (Table S2), the highest Co (1.59%) and Ni (0.9%) contents are obtained for CoDNi-N/C.

The N 1 s spectra are deconvoluted into pyridinic-N (~399 eV) and graphitic-N (401 eV), respectively (Fig. 3D). It has been well reported that more likely the carbon atoms with Lewis basicity next to pyridinic N are important active sites for the ORR [55–57]. The pyridinic-N content increases from 4.01% to 6.46% and 5.56% after adding PNi and DNi, respectively. Similar trends are found in graphitic-N, the content increases from 3.23% to those of 3.83% and 3.47% (Table S2), respectively. The Co 2p spectra (Fig. 3E) exhibit the metallic Co (778.6 for $2p_{3/2}$ and 794 eV for $2p_{1/2}$) and Co-N species (780.8 eV for $2p_{3/2}$ and 796.2 eV for $2p_{1/2}$) in all catalysts, which are further confirmed by the weak Co 2p satellite peaks (786.5 and 803.3 eV). The contents of Co-N species in CoPNi-N/C (1.33%) and CoDNi-N/C (1.29%) are all higher than those of Co-N/C (0.90%). Co-N species content increases significantly after the introduction of Ni complexes, indicating the anchoring effect of Co-Ni alloy. The Ni 2p spectra (Fig. 3F) shows the

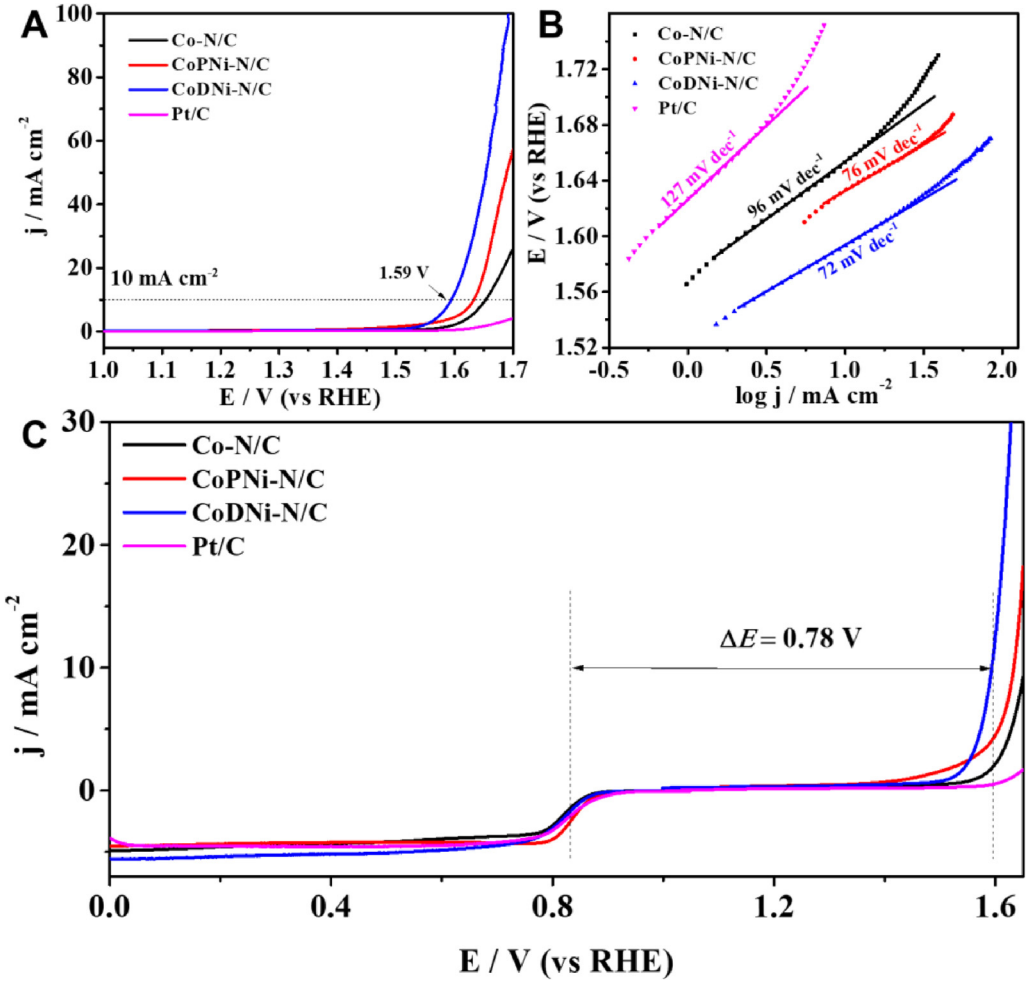

Fig. 5. (A) LSV curves of Pt/C, Co-N/C, CoPNi-N/C and CoDNi-N/C in O_2-saturated 0.1 M KOH solution and (B) corresponding Tafel plots, and (C) comparison of ORR and OER bifunctional activities of Co-N/C, CoPNi -N/C and CoDNi-N/C.

presence of metallic nickel (853.9 and 870.9 eV for $2p_{3/2}$ and $2p_{1/2}$, respectively) and Ni-N species (855.8 and 872.8 eV for $2p_{3/2}$ and $2p_{1/2}$, respectively), and the corresponding Ni 2p satellite peaks at 862 eV and 880 eV, respectively. Here, the content of Ni-N species achieves 0.69% for CoDNi-N/C and 0.20% for CoPNi-N/C, indicating the coordination effect is existed between nickel and imidazole ligand. The M-N-C (M = Co or Ni) species can serve as active sites and are beneficial to their performance in ORR catalysis [58–62]. The content of metallic Ni of CoDNi-N/C and CoPNi-N/C are 0.21% and 0.02%, which is attributed to the formation of Co-Ni alloy.

3.3. Electrocatalytic activity analysis

The electrocatalytic activities of the as-synthesized electrocatalysts toward ORR were investigated by CV and LSV in both O_2-saturated 0.1 M KOH and 0.1 M $HClO_4$ solutions, and the results were compared with those of commercial Pt/C (Figs. S7 and S8). It is worth noting that the reduction peak potential and onset potential are both shifted positively after adding Ni complex. Importantly, both well-defined cathodic peaks of CoPNi-N/C clearly appear at around 0.81 and 0.70 V in 0.1 M KOH and in 0.1 M $HClO_4$ respectively, and those of 0.82 and 0.71 V for CoDNi-N/C, which are more positive than those of Co-N/C (0.77 and 0.65 V), and close to those of Pt/C (0.84 and 0.75 V). Rotating disk electrode (RDE) voltammetries of different electrocatalysts at a rotation rate of 1600 rpm are carried out and the parameters of onset potential, half-wave potential ($E_{1/2}$) and cathodic current density are derived for comparison (Fig. 4A and C). It can be clearly observed that CoPNi-N/C is the best ORR electrocatalyst in both alkaline and acid media, showing an onset potential of 0.93 and 0.86 V and corresponding half-wave potential of 0.84 and 0.73 V, respectively. In parallel, the onset potential of CoDNi-N/C (0.92 V) is a little bit lower than that of CoPNi-N/C in alkaline solution, while greater current density (5.6 mA cm^{-2} at 0.4 V) can be observed, indicating it has close activity as CoPNi-N/C. The better ORR activity and actually catalytic kinetics could also be confirmed by a lower Tafel slope. As shown in Fig. 4B and D, the Tafel plots of CoPNi-N/C are 43 and 61 mV dec^{-1} in alkaline and acid solution, and those of CoDNi-N/C are 53 and 48 mV dec^{-1}, respectively, much lower than that of Pt/C (70 and 72 mV dec^{-1}). This superior ORR activity of CoPNi-N/C and CoDNi-N/C is among the best reported electrocatalysts (see Tables S3 and S4 for further comparison).

CoPNi-N/C was represented to investigate the ORR properties. RRDE technique is used to reveal the formation of intermediate products during ORR process and the number of electrons transferred (n). Figs. S9 A&B showed that the measured yields of HO_2^-/H_2O_2 for CoPNi-N/C are below 20%, giving n of 3.9 and 3.6 in alkaline and acid condition, respectively. These are consistent with the results obtained from the Koutecky-Levich (K–L) plots (Fig. S9 C&D), indicating a dominant four-electron ORR pathway of CoPNi-N/C. This is assigned to the high activity of Co and Ni atoms.

The poison tolerance of the catalysts is important for their practical applications. The tolerance toward methanol was determined by the chronoamperometric response at 0.6 V in both alkaline and acid conditions with a rotation rate of 1600 rpm (Fig. S10A and B). A sharp decrease in the current density was observed in the case of the

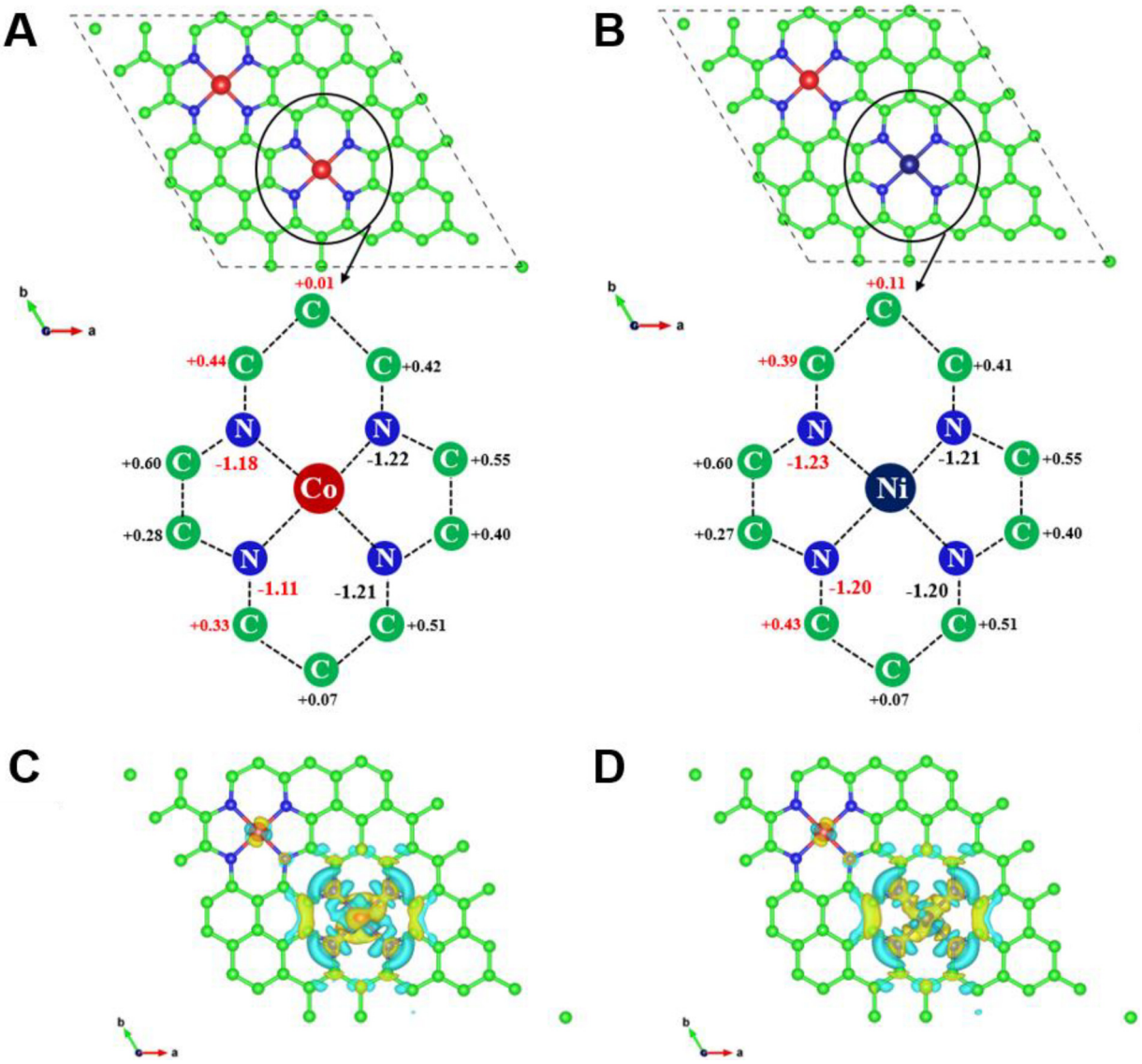

Fig. 6. Change of Bader charge in Co-N/C (A) and CoXNi-N/C (B) models. Plane-averaged electron density difference of Co-N/C (C) and CoXNi-N/C (D) models. Yellow and cyan areas represent electron accumulation and depletion. Respectively, the isosurface value is 0.003 eÅ^{-3}. (For interpretation of the references to colour in this figure legend, the reader is referred to the web version of this article).

commercial Pt/C catalyst, suggesting the methanol electro-oxidation and its sensitivity to the fuel crossover effect. Contrastively, CoPNi-N/C showed only a small attenuation in current upon the addition of 3 M of methanol, suggesting good tolerance to the crossover effect of the methanol. As traditional metal itself has poor tolerance to methanol interference, the good poison tolerance of CoPNi-N/C can be attributed to the abundant micro-porous carbon structure that could enhance the smooth diffusion rate of the electrolyte.

In addition, OER activities of the as-prepared electrocatalysts were also investigated in 0.1 M KOH solution. As shown in Fig. 5A and B, CoDNi-N/C provides an onset potential of 1.54 V vs. RHE (overpotential of 310 mV) and generates a current density of 10 mA cm^{-2} at a potential of 1.59 V vs. RHE (overpotential of 360 mV), which is superior to other commonly reported noble-metal-free and Pt/C electrocatalysts. Moreover, the CoDNi-N/C shows larger current density (53 mA cm^{-2} at 1.65 V) than that of CoPNi-N/C (18 mA cm^{-2} at 1.65 V), Co-N/C (9 mA cm^{-2} at 1.65 V) and commercial Pt/C (2 mA cm^{-2} at 1.65 V), indicating a superior electrocatalytic OER performance. The corresponding Tafel slope of CoDNi-N/C is 72 mV dec^{-1}, smaller than those of CoPNi-N/C Co-N/C and Pt/C. This is attributed to the abundant Co/Ni atoms and Co-N and Ni-N bond species in CoDNi-N/C. Besides, the ORR/OER bifunctional electrocatalytic activity of a given catalyst is usually evaluated by the overvoltage (ΔE) between E_{OER} (the potential at a current density of 10 mA cm^{-2} during water oxidation) and E_{ORR} (the half-wave potential during oxygen reduction), which translates into loss in efficiency. As shown in Fig. 5C, smaller overvoltage value of CoDNi-N/C (0.78 V) and CoPNi-N/C (0.79 V) indicate competitive bifuntional electrocatalytic activity and potential for practical application (see Table S5 for further comparison, including single atom catalysts).

To evaluate the stability of CoXNi-N/C, accelerated durability tests (ADT) are performed by continuous potential cycling. Take CoPNi-N/C as an example, the polarization curves for ORR after 5000 ADT cycles retain more than 85% of its initial current density at ~0.8 V with only 14 (in 0.1 M KOH) and 11 mV (in 0.1 M $HClO_4$) negative shift in $E_{1/2}$ (Fig. S11A and B); The polarization curve for OER (in 0.1 M KOH) after 5000 ADT cycles show larger current density at 1.7 V and the overpotential improve 20 mV (Fig. S11C). These results indicated the great stability of CoPNi-N/C.

3.4. Discussion

From the experiment results illustrated above, it is obviously that atomic Co/Ni dual sites significantly improved the electrocatalytic activities of porous Janus-like carbon materials. Both metallic Co/Ni alloy nanoparticles and atomic Co/Ni dispersed sites contribute to the electrocatalytic activities in different aspects.

To investigate electrocatalytic activity of catalysts, quantum mechanical calculations were carried out to obtain the electronic properties using DFT method. Structures of pure nitrogen doped carbon, single Co/Ni and dual Co/Ni atomic dispersed nitrogen doped carbon have been constructed for simulation as illustrated in Figs. 6 and S12. The Bader charge (Table S6) revealed that two N-atoms in Co-Ni system become more negative after Ni atom immobilized into the carbon matrix. In Co-N/C system, the two N-atoms gain 1.18 and 1.11 electrons (Fig. 6A), while the two N-atoms in CoXNi-N/C system gain 1.23 and 1.20 electrons (Fig. 6B), respectively. This exhibits Ni-N bonds have obvious covalent character and can increase the electronic activity of N atoms. The difference of plane-averaged electron density can be used to illustrate the transmission of electrons on the interface. The following formulas were used to evaluate the plane-averaged electron density:

$$\Delta\rho = \rho_{\text{Co-N/C}} - \rho_{\text{Co}}\text{-N-C} - \rho_{\text{Co}},$$

$$\Delta\rho = \rho_{\text{CoXNi-N/C}} - \rho_{\text{Co}}\text{-N-C} - \rho_{\text{Ni}},$$

where $\rho_{\text{Co-N/C}}$ and $\rho_{\text{CoXNi-N/C}}$ are the plane-averaged density of Co-N/C and CoXNi-N/C, ρ_{Co}-N-C and $\rho_{\text{Co/Ni}}$ are the individual plane-averaged densities of Co-N-C and Co/Ni. As shown in Figs. 6C&D and S13, charge redistribution appears around the middle of Co/Ni atom, and a few electrons lose in the Co-N/C system, explains that CoXNi-N/C system is more reductive than Co-N/C system.

It is noted that the precursors play key roles in the properties of Janus-like carbon frameworks. For instance, CoPNi-N/C has abundant micro-porosity of 41.72%, much higher than that of CoDNi-N/C. High content of micropores is beneficial to its absorption of oxygen molecules and thus lower the activation energy for ORR. Thus CoPNi-N/C showed better performance than CoDNi-N/C in ORR. On the other hand, CoDNi-N/C has much higher metallic Co/Ni content than CoPNi-N/C (see Table S2). As metallic nanoparticles are believed to be the active species for OER, high content of metallic Co/Ni alloy will certainly result in the better OER performance [63]. Thus, CoDNi-N/C and CoPNi-N/C shows different activities towards ORR and OER.

4. Conclusions

In summary, we developed an universal and effective strategy for designing multiatomic Janus-like electrocatalysts by using precursors of different topology structures. Specifically, atomic Co/Ni dual sites immobilized N-doped porous Janus-like carbon frameworks were synthesized through coordinating ZIF-67 with Ni complexes (PNi and DNi). The obtained electrocatalysts showed homogeneous atom-level Co/Ni dual active sites. The electrocatalysts performed good catalytic activities towards ORR in both acidic and basic media due to abundant content of micropores and nitrogen. They can also use as bifunctional electrocatalyst with good OER performance due to newly introduced nickel. Finally, the account of good ORR/OER performance of atomic Co/Ni dual sites is explored by DFT calculation, and Ni-N bonds are proved to increase the electronic activity of N atoms. This work paves an avenue for developing efficient multiatomic Janus-like electrocatalysts for energy conversion.

Acknowledgements

This work was supported by a grantfrom the National Natural Science Foundation of China (No. 91545125, U1662121, 51425405, 51402298, and 51608509), the National High Technology Research and Development Program of China (863 Program) (No. 2014AA06A513), Youth Innovation Promotion Association of CAS, Postdoctoral Science Foundation (No. 2016M590670), Natural Science Foundation of Shandong Province (No. ZR2016EEB25), Alexander von Humboldt Foundation Postdoctoral Research Fellowship (No. 1186323), Beijing Municipal Commission Educationand Cross training plan for high level talents in Beijing colleges and universities (KM201710015009). Tsinghua Qingfeng Scholarship (THQF2018-16). We are indebted to associate professor Qian Guo for her detailed review of and comments on the manuscript.

Appendix A. Supplementary data

Supplementary material related to this article can be found, in the online version, at doi:https://doi.org/10.1016/j.apcatb.2018.08.074.

References

[1] W. Xia, A. Mahmood, Z. Liang, R. Zou, S. Guo, Angew. Chem. Int. Ed. 55 (2016) 2650–2676.
[2] L.M. Dai, Y.H. Xue, L.T. Qu, H.J. Choi, J.B. Baek, Chem. Rev. 115 (2015) 4823–4892.
[3] T.Y. Ma, S. Dai, M. Jaroniec, S.Z. Qiao, J. Am. Chem. Soc. 136 (2014) 13925–13931.
[4] J.C. Li, P.X. Hou, S.Y. Zhao, C. Liu, D.M. Tang, M. Cheng, F. Zhang, H.M. Cheng, Energy Environ. Sci. 9 (2016) 3079–3084.
[5] Y. Nie, L. Li, Z.D. Wei, Chem. Soc. Rev. 44 (2015) 2168–2201.
[6] J.T. Zhang, Z.H. Zhao, Z.H. Xia, L.M. Dai, Nat. Nanotechnol. 10 (2015) 444–452.
[7] B.Y. Xia, Y. Yan, N. Li, H.B. Wu, X.W. Lou, X. Wang, Nat. Energy 1 (2016) 15006.
[8] C. Hu, L. Dai, Angew. Chem. Int. Ed. 55 (2016) 11736–11758.
[9] Y. Chen, S. Ji, C. Chen, Q. Peng, D.S. Wang, Y.D. Li, Joule 2 (2018) 1242–1264.
[10] S. Dilpazir, H. He, Z. Li, M. Wang, P. Lu, R. Liu, Z. Xie, D. Gao, G. Zhang, ACS Appl. Energy Mater. 1 (2018) 3283–3291.
[11] H.B. Yang, J. Miao, S.F. Hung, J. Chen, H. Tao, X. Wang, L. Zhang, R. Chen, J. Gao, H. Chen, L.M. Dai, B. Liu, Sci. Adv. 2 (2016) e1501122-el501122.
[12] E. Bayram, J. Lu, C. Aydin, N.D. Browning, S. Özkar, E. Finney, B.C. Gates, R.G. Finke, ACS Catal. 5 (2015) 3514–3527.
[13] J. Wang, Z.Q. Huang, W. Liu, C.R. Chang, H.L. Tang, Z.J. Li, W.X. Chen, C.J. Jia, T. Yao, S.Q. Wei, Y. Wu, Y.D. Li, J. Am. Chem. Soc. 139 (2017) 17281–17284.
[14] P.Q. Yin, T. Yao, Y. Wu, L.R. Zheng, Y. Lin, W. Liu, H.X. Ju, J.F. Zhu, X. Hong, Z.X. Deng, G. Zhou, S.Q. Wei, Y.D. Li, Angew. Chem. Int. Ed. 55 (2016) 10800–10805.
[15] Z. Li, Y. Jiang, C. Liu, Z. Wang, Z. Cao, Y. Yuan, M. Li, Y. Wang, D. Fang, Z. Guo, D. Wang, G. Zhang, J. Jiang, Environ. Sci. Nano 5 (2018) 1834–1843.
[16] C. Zhao, H. Yu, J. Wang, W. Che, Z. Li, T. Yao, W. Yan, M. Chen, J. Yang, S. Wei, Y. Wu, Y.D. Li, Mater. Chem. Front. 2 (2018) 1317–1322.
[17] C. Zhao, X. Dai, T. Yao, W. Chen, X. Wang, J. Wang, J. Yang, S. Wei, Y. Wu, Y.D. Li, J. Am. Chem. Soc. 139 (2017) 8078–8081.
[18] Y. Han, Z. Wang, R. Xu, W. Zhang, W. Chen, L. Zheng, J. Zhang, J. Luo, K. Wu, Y. Zhu, C. Chen, Q. Peng, Q. Liu, P. Hu, D.S. Wang, Y.D. Li, Angew. Chem. 130 (2018) 1962–1966.
[19] J.T. Zhang, Z.H. Zhao, Z.H. Xia, L.M. Dai, Nat. Nanotechnol. 10 (2015) 444–452.
[20] S. Cai, Z. Meng, H. Tang, Y. Wang, P. Tsiakara, Appl. Catal. B Environ. 207 (2017) 477–484.
[21] Y. Yu, Y. Yu, H.B. Wu, X.W. Lou, Angew. Chem. Int. Ed. 54 (2015) 5331–5335.
[22] S. Zhao, B. Rasimick, W. Mustain, H. Xu, Appl. Catal. B Environ. 203 (2017) 138–145.
[23] J.F. Yao, H.T. Wang, Chem. Soc. Rev. 43 (2014) 4470–4493.
[24] Y. Han, Y.G. Wang, W. Chen, R. Xu, L. Zheng, J. Zhang, J. Luo, R.A. Shen, Y. Zhu, W.C. Cheong, C. Chen, Q. Peng, D.S. Wang, Y.D. Li, J. Am. Chem. Soc. 139 (2017) 17269–17272.
[25] Y. Chen, S. Ji, Y. Wang, J. Dong, W. Chen, Z. Li, R. Shen, L. Zheng, Z. Zhuang, D.S. Wang, Y.D. Li, Angew. Chem. Int. Ed. 56 (2017) 6937–6941.
[26] Z. Li, W. Wang, H. Cao, Q. Zhang, X. Zhou, D. Wang, Y. Wang, S. Zhang, G. Zhang, C. Liu, Y. Zhang, R. Liu, J. Jiang, Adv. Mater. Technol. 2 (2017) 1700224.
[27] Z. Li, L. Yang, H. Cao, Y. Chang, K. Tang, Z. Cao, J. Chang, Y. Cao, W. Wang, M. Gao, C. Liu, D. Liu, H. Zhao, Y. Zhang, M. Li, Carbohydr. Polym. 175 (2017) 223–230.
[28] Y.P. Zhu, T.Y. Ma, M. Jaroniec, S.Z. Qiao, Angew. Chem. Int. Ed. 56 (2017) 1324–1328.
[29] A. Aijaz, J. Masa, C. Rosler, W. Xia, P. Weide, A.J.R. Botz, R.A. Fischer, W. Schuhmann, M. Muhler, Angew. Chem. Int. Ed. 55 (2016) 4087–4091.
[30] F.L. Meng, H.X. Zhong, D. Bao, J.M. Yan, X.B. Zhang, J. Am. Chem. Soc. 138 (2016) 10226–10231.
[31] J. Wei, Y. Hu, Y. Liang, B. Kong, J. Zhang, J. Song, Q. Bao, G.P. Simon, S.P. Jiang, H. Wang, Adv. Funct. Mater. 25 (2015) 5768–5777.
[32] A. Han, W. Chen, S. Zhang, M. Zhang, Y. Han, J. Zhang, S. Ji, L. Zheng, Y. Wang, L. Gu, C. Chen, Q. Peng, D.S. Wang, Y.D. Li, Adv. Mater. 30 (2018) 1706508.
[33] Y. Han, Y. Wang, R. Xu, W. Chen, L. Zheng, A. Han, Y. Zhu, J. Zhang, H. Zhang, J. Luo, C. Chen, Q. Peng, D.S. Wang, Y.D. Li, Energy Environ. Sci. (2018), https://

doi.org/10.1039/c8ee01481g.
[34] T. Zhang, J. Du, H. Zhang, C. Xu, Electrochim. Acta 219 (2016) 623–629.
[35] B. Chen, G. Ma, Y. Zhu, J. Wang, W. Xiong, Y. Xia, J. Power Sources 334 (2016) 112–119.
[36] D. Zhao, J.L. Shui, L.R. Grabstanowicz, C. Chen, S.M. Commet, T. Xu, J. Lu, D.J. Liu, Adv. Mater. 26 (2014) 1093–1097.
[37] L. Shang, H. Yu, X. Huang, T. Bian, R. Shi, Y. Zhao, G.I.N. Waterhouse, L.Z. Wu, C.H. Tung, T. Zhang, Adv. Mater. 28 (2016) 1668–1674.
[38] J. Wei, Y.X. Hu, Y. Liang, B.A. Kong, J. Zhang, J.C. Song, Q.L. Bao, G.P. Simon, S.P. Jiang, H.T. Wang, Adv. Funct. Mater. 25 (2015) 5768–5777.
[39] W. Xia, R.Q. Zou, L. An, D.G. Xia, S.J. Guo, Energy Environ. Sci. 8 (2015) 568–576.
[40] J. Yang, D. He, W. Chen, W. Zhu, H. Zhang, S. Ren, X. Wang, Q. Yang, Y. Wu, Y.D. Li, ACS Appl. Mater. Interfaces 9 (2017) 39450–39455.
[41] H.L. Peng, F.F. Liu, X.J. Liu, S.J. Liao, C.H. You, X.L. Tian, H.X. Nan, F. Luo, H. Song, Z.Y. Fu, P.Y. Huang, ACS Catal. 4 (2014) 3797–3805.
[42] L.L. Zhang, J. Xiao, H.Y. Wang, M.H. Shao, ACS Catal. 7 (2017) 7855–7865.
[43] B.Y. Guan, L. Yu, X.W. Lou, Energy Environ. Sci. 9 (2016) 3092–3096.
[44] F.D. Speck, K.E. Dettelbach, R.S. Sherbo, D.A. Salvatore, A. Huang, C.P. Berlinguette, Chemical 2 (2017) 590–597.
[45] C. Tang, H.F. Wang, H.S. Wang, F. Wei, Q. Zhang, J. Mater. Chem. A 4 (9) (2016) 3210–3216.
[46] L. Ma, C.M. Wang, B.Y. Xia, K.K. Mao, J.W. He, X.J. Wu, Y.J. Xiong, X.W. Lou, Angew. Chem. Int. Ed. 54 (2015) 5666–5671.
[47] G.Q. Zhang, B.Y. Xia, X. Wang, X.W. Lou, Adv. Mater. 26 (2014) 2408–2412.
[48] M. Yu, D.R. Trinkle, J. Chem. Phys. 134 (2011) 064111.
[49] J. Hafner, J. Comput. Chem. 29 (2008) 2044–2078.
[50] J.P. Perdew, J.A. Chevary, S.H. Vosko, K.A. Jackson, M.R. Pederson, D.J. Singh, C. Fiolhais, Phys. Rev. B 46 (1992) 6671.
[51] J.P. Perdew, Y. Wang, Phys. Rev. B 45 (1992) 13244.
[52] R. Banerjee, A. Phan, B. Wang, C. Knobler, H. Furukawa, M. O'Keeffe, O.M. Yaghi, Science 319 (2008) 939–943.
[53] J. Tang, R.R. Salunkhe, J. Liu, N.L. Torad, M. Imura, S. Furukawa, Y. Yamauchi, J. Am. Chem. Soc. 137 (2015) 1572–1580.
[54] V. Beermann, M. Gocyla, E. Willinger, S. Rudi, M. Heggen, R.E. Dunin-Borkowski, M.G. Willinger, P. Strasser, Nano Lett. 16 (2016) 1719–1725.
[55] D.H. Guo, R. Shibuya, C. Akiba, S. Saji, T. Kondo, J. Nakamura, Science 351 (2016) 361–365.
[56] T.Y. Ma, J.L. Cao, M. Jaroniec, S.Z. Qiao, Angew. Chem. Int. Ed. 55 (2016) 1138–1142.
[57] H. C, L. M. Dai, Adv. Mater. 2016, 1604942.
[58] T.Y. Yung, L.Y. Huang, T.Y. Chan, K.S. Wang, T.Y. Liu, P.T. Chen, C.Y. Chao, L.K. Liu, Nanoscale Res. Lett. 9 (2014) 444.
[59] H. Lei, Z. Song, D.L. Tan, X.H. Bao, X.H. Mu, B.N. Zong, E.Z. Min, Appl. Catal. A Gen. 214 (2001) 69–76.
[60] C. Padeste, D.L. Trimm, R.N. Lamb, Catal. Lett. 17 (1993) 333–339.
[61] C. Tang, Q. Zhang, J. Mater. Chem. A 4 (2016) 4998–5001.
[62] Y. Liu, H. Jiang, Y. Zhu, X. Yang, C. Li, J. Mater. Chem. A 4 (2016) 1694–1701.
[63] B. Chen, X. He, F. Yin, H. Wang, D. Liu, R. Shi, J. Chen, H. Yin, Adv. Funct. Mater. (2017) 1700795.